ELSEVIER

Polymer Vol. 37 No. 9, pp. 1607–1619, 1996

0032-3861/96/$15.00 + 0.00

Influence of particle–craze interactions on the sub-critical fracture of core–shell HIPS

C. Maestrini* and L. Monti
Enichem Research Centre, Via Taliercio 14, 46100 Mantova, Italy

and H. H. Kausch
Laboratoire de Polymères – Departement de Materiaux, Ecole Polytechnique Fédérale de Lausanne, Ecublens, 1015 Lausanne, Switzerland

High impact polystyrene (HIPS) particles with sizes well below 1 μm have been demonstrated to interact with growing crazes giving rise to some local, non-catastrophic fibril texture damage, which increases with increasing particle size and volume fraction of the second phase. The influence of such damage on the sub-critical fracture behaviour of some core–shell HIPSs, which have been well characterized from the morphological and structural points of view, is investigated. A statistical craze fibril fracture model is adopted that considers a two-parameter Weibull distribution and a Paris law for the sub-critical crack advance is derived. The meaning and dependence of the Weibull parameters on the structural and morphological characteristics of the considered materials are discussed. The proposed approach is not limited to the statistical idea and can, in principle, be used to derive the Paris behaviour in a larger class of materials. Copyright © 1996. Published by Elsevier Science Ltd.

(Keywords: high impact polystyrene; rubber particles; crazing)

INTRODUCTION

It has long been recognized that fracture in polystyrene (PS) follows the formation of crazes and originates in the breakdown of the craze fibrils[1,2]. The increase in toughness of high impact polystyrene (HIPS), with respect to the PS homopolymer, is related to the effects of the rubbery particles, ordinarily composed of polybutadiene (PB), on the crazing mechanism. It is generally agreed that the rubbery particles can act: (1) as craze initiators, promoting the nucleation of several crazes[3,4]; and (2) as craze terminators, avoiding the too rapid changeover of crazes into cracks[3,4].

Recently, evidence of a different microscopic interaction between the growing crazes and small particles has been reported: in the phenomenon, designated as entrapping, the particles are drawn into fibrillar texture of crazes, without any contribution to the nucleation and termination of crazes[5]. The rubber particles can come in contact either with the craze–bulk interface during the drawing mechanism, or with the advancing craze tip. In the first case they are said to be driven inside the craze by the same force that controls the fibril growth, while in the second case they should experience an extremely large deformation and, consequently, break down. Some local fibril breakdown can take place due to the entrapped particles. The entrapping phenomenon is evident when the particle size is well below 1 μm.

Because of the fact that entrapping does not seem to produce catastrophic fracture of the craze, it is possible to think that its effects could be investigated in the fracture propagation phase, giving the opportunity to study the relationships existing between the macroscopic sub-critical fracture propagation behaviour and the morphological and structural characteristics of the microscopic plastic and damage processes.

* To whom correspondence should be addressed

EXPERIMENTAL ANALYSIS AND DISCUSSION

Materials

We chose to analyse seven different HIPSs, indicated in the following by the letters A to G, all characterized by the presence of sub-micrometre rubber particles having a core–shell structure (*Figures 1* and *2*). They are produced following usual suspension polymerization techniques, modified by the presence of PS–PB copolymer in the initial solution. If styrene is polymerized in the presence of dissolved block copolymers, their domains are preserved in solution in the form of micelles and these micelles somehow retain the structure of the parent block copolymer. Additional grafting onto the PB part of the block copolymer leads to a higher PS content in the ordered micelles. If this PS content exceeds a certain critical limit, the structure of the micelles changes according to the corresponding structural change in the parent block copolymer, as if it had a higher PS content from the beginning. When this change happens before phase inversion, the type of particles generated afterwards corresponds to the new micelle structure that, in our case, was always that of a core–shell particle[6,7].

Table 1 contains a summary of the molecular and structural parameters measured by means of common characterization methods (described in table footnotes) for

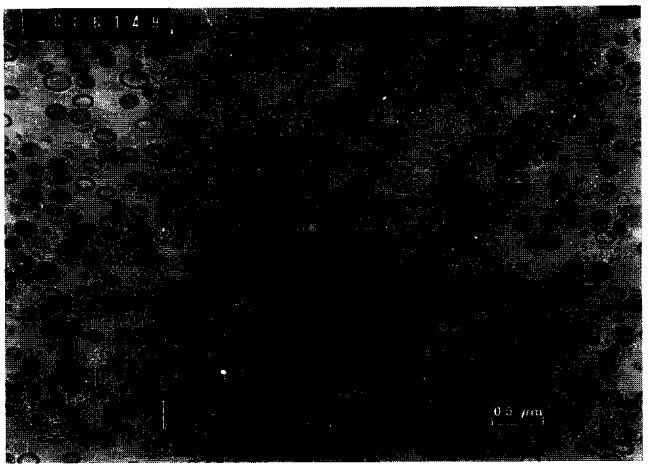

Figure 1 TEM picture of material A, obtained from a slice having a thickness of approximately 90 nm

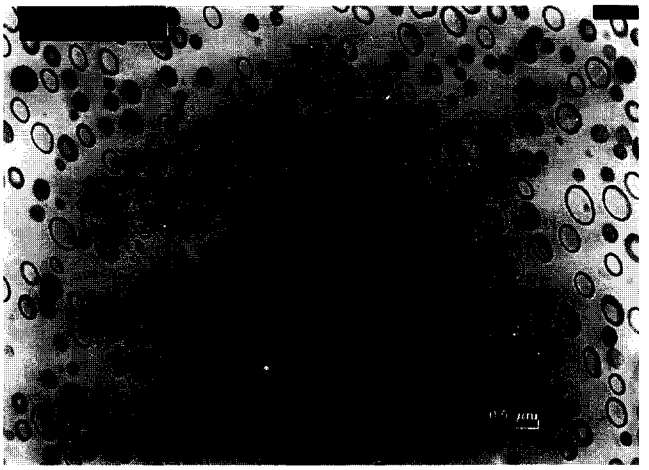

Figure 2 TEM picture of material G, obtained from a slice having a thickness of approximately 90 nm

Table 1 General parameters of HIPS samples studied

	A	B	C	D	E	F	G	X
M_w[a]	172 000	152 000	150 000	151 000	158 500	157 000	160 000	160 000
M_w/M_n[b]	2.04	1.82	1.89	1.91	1.90	1.88	1.91	1.92
PB[c]	8.6	8.4	–	9.1	8.9	8.6	8.7	–
Gel[d]	27.3	28.8	26.7	26.5	32.6	27.9	27.9	–
Swelling index[e]	14.6	13.5	16.0	18.3	10.0	12.6	14.2	–
Izod strength[f]	38	55	51	41	53	56	55	~20

[a] M_w: weight-average molecular weight of PS ($g\,mol^{-1}$) determined by gel permeation chromatography (g.p.c.) with a refractive index detector on tetrahydrofuran evolution of the soluble part
[b] M_w/M_n: polydispersity index of PS, measured as the ratio between the weight-average molecular weight (M_w) and the average molecular weight (M_n) by g.p.c. (see above)
[c] PB: weight fraction of PB (%) measured by titration methods
[d] Gel: second-phase weight fraction (%) measured by phase separation methods in selective solvent (the samples were dissolved and washed in methyl ethyl ketone (MEK), the insoluble part was separated by centrifugation, precipitated by ethanol and then filtered, dried and weighed)
[e] Swelling index: weight ratio between swollen and dry gel (%). The dry gel is the one measured as above, the swollen gel is weighed after 5 h from the centrifugation, but before the precipitation
[f] Izod strength ($J\,m^{-1}$): obtained following the ASTM D256 protocol on injection moulded specimens

the materials considered. A PS homopolymer, indicated by the letter X, having molecular characteristics similar to those of the HIPS matrices is added to complete the data.

In order to realize a precise and quantitatively useful structural characterization, accurate determination of the second phase volume fraction (*SPVF*) and the particle size distribution (*PSD*) is necessary. The ordinary way of measuring these two key parameters is, in fact, subjected to some criticism and gives rise to data that cannot be considered realistic[8–10]. For this reason, we adopted the stereological approach described in detail in refs 8 and 9. This method consists in analysing transmission electron microscopy (TEM) pictures, obtained following the standard technique reported in ref. 11, from material slices having different thicknesses and then reconstructing the bulk situation. We used the following equations[9]:

$$\langle r^1\rangle = \frac{\pi\langle R^2\rangle + 2t\langle R^1\rangle}{4\langle R^1\rangle + 2t} \tag{1}$$

$$\langle r^2\rangle = \frac{4\langle R^3\rangle + 3t\langle R^2\rangle}{6\langle R^1\rangle + 3t} \tag{2}$$

$$\phi_{app} = \frac{4\langle R^3\rangle + 3t\langle R^2\rangle}{4\langle R^3\rangle}\cdot\phi \tag{3}$$

where $\langle r^i\rangle$ represents the ith moment of the particle radius distribution in the TEM images, $\langle R^j\rangle$ the jth moment of the real particle distribution in the bulk, t the observed section thickness, ϕ_{app} the apparent *SPVF* in the TEM images and ϕ the real *SPVF*. Equations (1), (2) and (3), which produce an over-determined system when one considers more than one thickness, have been solved using a simple algorithm, which has been previously discussed in ref. 10, and consists in the minimization of the maximum components of a normalized linear error function containing all the parameters $\langle R^j\rangle$ and ϕ.

In *Table 2* the results of such a characterization are displayed. In the remainder of this paper, when discussing *SPVF* (indicated by ϕ) we will always refer to the data coming from this stereological approach. From *Table 2* it is immediately noticeable that the *PSD* is almost exactly monomodal for all the materials: the parameter β, defined as

$$\beta = \sqrt{\frac{\langle R^2\rangle}{\langle R^1\rangle^2} - 1} \tag{4}$$

and representing the dispersion of the distribution (the larger β, the broader the distribution), being always extremely close to zero. This is very convenient because it

Table 2 Data from the stereological characterization[a]

	A	B	C	D	E	F	G
$\langle r^1\rangle_1$	68	78	80	76	90	88	89
$\langle r^2\rangle_1$	5000	6600	7000	6300	8800	8500	8700
$\phi_{app\,1}$	30.8	34.5	35.1	32.2	37.5	32.5	35.0
$\langle r^1\rangle_2$	70	77	80	79	93	89	94
$\langle r^2\rangle_2$	5300	6400	7100	6600	9300	8600	9700
$\phi_{app\,2}$	36.0	35.2	38.2	36.6	40.5	37.7	38.0
$\langle r^1\rangle_3$	74	81	84	78	91	92	91
$\langle r^2\rangle_3$	5900	7000	7700	6600	9000	9200	9100
$\phi_{app\,3}$	36.8	39.4	40.4	40.0	42.5	40.8	38.2
$\langle R^1\rangle$	79	88	92	87	103	102	103
β^2	0.001	0.004	0.000	0.000	0.001	0.000	0.018
ϕ	13.8	15.7	17.2	15.3	18.9	17.3	17.5

[a] The meaning of the symbols is given in the text. Subscripts 1, 2 and 3 refer to slice thickness of 120, 170 and 215 nm, respectively. For every slice thickness a population of at least 1000 particles was considered. $\langle r^1\rangle$ and $\langle R^1\rangle$ are in nm, $\langle r^2\rangle$ are in nm^2, ϕ_{app} and ϕ are in %

Table 3 Measured elastic and plastic parameters[a]

	A	B	C	D	E	F	G
μ	881	774	–	819	728	791	777
E	2007	1853	–	2105	1837	2024	2053
σ_y	24.89 ± 0.07	19.83 ± 0.06	–	20.08 ± 0.22	20.34 ± 0.17	20.18 ± 0.27	19.52 ± 0.17

[a] The meaning of the symbols is given in the text. Moduli and stresses are in MPa

allows us to consider the effect of only the mean particle size on the mechanical behaviour, disregarding possible complications due to large distributions. So, in the following, we will always refer only to the average particle radius, which coincides with the first moment of the distribution, and we will indicate it simply as R.

Table 3 contains experimental data for the shear modulus μ and the Young's modulus E for the HIPS materials considered. E and μ were measured on compression moulded specimens adopting a three-point bending and a simple torsion geometry, respectively, both in dynamic regime with sinusoidal strain pulses at a frequency of 1 Hz with the maximum strain achievable in the linear viscoelastic zone. In *Table 3* the values of the yielding stresses for the considered materials are also reported. The yielding experiments were performed in tension on compression moulded specimens having dimensions of 45 mm (gauge length) × 10 mm × 2 mm, at a nominal strain rate of $4 \times 10^{-4}\,s^{-1}$. The yielding point, σ_y, was considered as the average on at least five measurements of the maximum in the stress–strain curve.

Microscopic examination of the craze features

Some of the first useful results from TEM observations of crazed materials are due to Kambour and co-workers[12,13]. They deformed bulk samples of poly(phenyl ether) (PPE) and HIPS, immersed them in an appropriate fluid in order to fill up the voids contained inside the crazes and then froze the systems to below the solidification point of the fluid. In this way it was possible to microtome the samples without destroying the intimate structure of the crazes, which, on the contrary, is what happens when microscopic post-mortem investigation is made. The thin slices were, eventually, observed using the TEM and the negative pressure inside the microscope column was sufficient to evaporate the fluid, restoring the craze original features. This technique, however, has a practical limitation: the choice of the appropriate fluid is extremely difficult. In the case of HIPS, for example, the fluid was a eutectic mixture of iodine and sulfur, whose solidification point was about 65°C. It is clear that the craze filling process took place at a temperature higher than this one and thus close to the glass transition temperature (T_g) of PS, introducing a potential healing of crazes and a consequent change in their structure.

Lauterwasser and Kramer[14] by-passed these problems by using films cast or drawn from solutions and bonded to annealed copper grids. Deforming the grids meant that no microtoming-after-deformation procedure was needed and the observation of fresh and undamaged crazes was possible. Low-angle electron diffraction (LAED) studies on films deformed in such a way and small-angle X-ray scattering (SAXS) on crazed bulk samples demonstrated that the structure of the crazes in PS in these two conditions is the same, when the thickness of films is at least 0.2 μm[15–17]. The copper grid technique (CGT) has been used in many studies, widely reviewed in refs 18 and 19, and gave the possibility to understand the microscopic and molecular aspects of crazing in PS and in several other polymers[20–24].

Donald and Kramer[24,25] used the same approach also to study the deformation mechanism in HIPS, but in this case the fact that the films were obtained from solutions introduced some difficulties. Systems like HIPS are only partially soluble: the crosslinked rubber particles do not dissolve and the original structure is hard to reproduce from casting or drawing; the spatial particle distribution is not well homogeneous and hence the effective *SPVF* is

hard to estimate. Again, the presence of residual solvent can lead to the particles remaining in a swollen state, thus changing their properties and sizes.

More practical and reliable, in our opinion, is utilization of the standard microtoming technique in order to prepare samples. Small slices so obtained can be easily bonded to treated copper grids by means of simple temperature cycles above T_g, as outlined in ref. 5, strained after annealing overnight at about 80°C and observed by TEM in a way similar to that described by Lauterwasser and Kramer. Due to the fact that suitable slices have a thickness of about 1 μm, a considerable apparent overlapping of rubber particles is visible in the TEM pictures, because of stereological reasons. In these conditions it is easy to calculate from equation (3) that, for a material having particles with mean radius of about 100 nm, as in the case of our HIPSs, an *SPVF* of about 10% gives rise to images in which the apparent volume fraction is 100%, which means that the pictures are completely covered by particles![8,9]. For this reason, for each material we realized a dilution with PS (material X in *Table 1*) having an *SPVF* of about 2.5%. The diluted materials will be indicated by an asterisk in the following, in order not to confuse them with the original ones.

After microtoming, each diluted material was prepared according to ref. 5 and strained at room temperature on a motorized microdynamometer with a strain rate of approximately $10^{-4}\,s^{-1}$, up to the maximum deformation reachable before fracture (2–3%). Crazes were always observable in the strained film, regions of which were cut and put in the TEM chamber without any staining. The largest observable crazes have been photographed in conditions of slight under-focus and under-exposure, in order to enhance the visual quality of the images, to obtain resolved Fourier spectra (see below) and not to saturate the chemical sensitivity of the photographic negatives.

Qualitative observation of the crazes substantially confirms what has already been reported about the phenomenon of entrapping of the small particles inside the crazes: it is difficult to say that the small particles act as craze initiators, while they are easily swallowed inside the craze texture, producing a variable degree of fibril breakdown. Broken particles are also observable. *Figures 3* and *4* show the different features of the crazes in core–shell HIPSs.

A quantitative analysis of the craze features is possible. It has previously been demonstrated that important parameters, such as the craze matter volume fraction with respect to the bulk, v_f, and the mean fibril diameter and spacing, indicated by D and D_0, respectively, can be extracted in different ways from the TEM images. Yang and Kramer[26] showed that an efficient way of analysing the TEM images is the computing of the Fourier transform (FT) of the one-dimensional optical density distribution of the TEM image plate along the axis perpendicular to the craze fibrils. This technique is extremely convenient in our case, in which the maximum thickness of the observable craze was of the order of 1 μm and, thus, well below the one suitable for an LAED pattern. At least 10 mature crazes from each material were photographed; five of them, reproduced on negatives at 15000× and chosen between those not showing a dramatic presence of fibril damaging

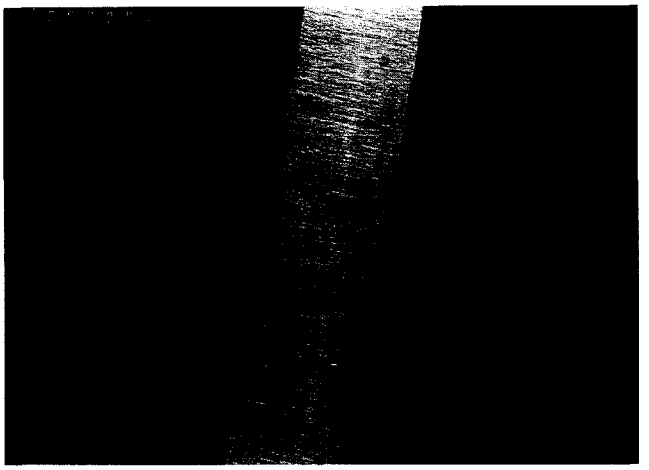

Figure 3 TEM picture of a craze in material A

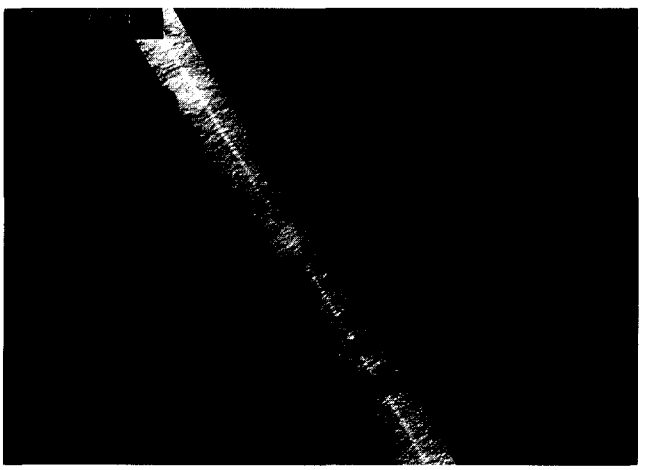

Figure 4 TEM picture of a craze in material G. Local fibril breakdown and broken particles are visible

phenomena, were then analysed by means of an optical microdensitometer using a 100 μm × 100 μm aperture; 10 traces of 1024 readings with a possible reading distance of 25, 50 or 70 μm on the picture, corresponding to 1.7, 3.3 and 4.6 nm on the craze, were obtained on each negative. The midrib[18] along the craze centre, which is produced by fibril drawing under stress concentration just behind the craze tip, has a much lower v_f and was always avoided, so that the data could be representative of the average craze microstructure. The traces were computed by a fast FT algorithm, generating a spectrum in the spatial frequency domain parallel to the axis perpendicular to the craze fibril (in the following the spatial frequency will be denoted by s, by analogy to the symbolism adopted for the scattering vector in diffraction experiments). The spectra were then averaged. The resulting average spectrum of the fibril images should show a maximum along the frequency axis, if there is any correlation among the fibril spacings, a fact that happened practically for every considered sample. *Figure 5* shows a typical spectrum.

Analysis of the spectra was performed following the method of Porod[27,28], as applied to crazes firstly by Brown[16]. The average fibril spacing D_0 is usually computed as the inverse of s_{max}, where s_{max} is the spatial

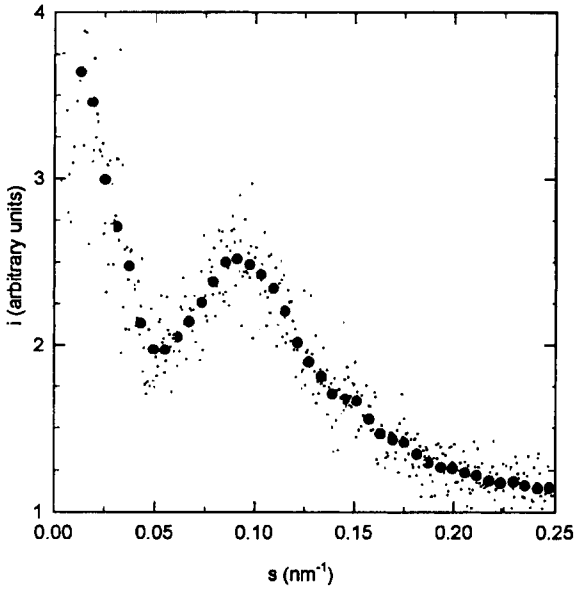

Figure 5 Average Fourier transform (FT) spectrum of 10 optical microdensitometric traces on a craze in material G (plot of the spectral intensity *i versus* the spatial frequency *s*). The dots represent data as they come from the FT algorithm, every circle is the average of 20 experimental dots

frequency at the relative maximum in the spectra. It is known that, due to the fact that the larger fibrils contribute more to the scattering intensity[16,17], D_0 is an overestimate of the true average fibril spacing. Maestrini and Kramer[29] showed that the factor involved in this overestimation is, for PS, about 1.5; in the following we will then indicate the value of the fibril spacing corrected by this factor as D_0^*.

The average fibril diameter D can be obtained from the two so-called scattering invariants, h_i and Q. For s values well above the relative maximum s_{max}, the Porod law applies:

$$i(s) = \frac{h_i}{s^3} + i_b \tag{5}$$

where $i(s)$ is the spectral intensity, i_b the background intensity (assumed to be independent of the fibril scattering[16]) and h_i the Porod's constant. The constant h_i and the background intensity i_b can be easily calculated from each spectrum simply by performing a linear regression on $i(s)s^3$ *versus* s^3. The value of i_b comes from the resulting slope and h_i from the y-intercept. The invariant Q is given by:

$$Q = 2\pi \int_0^\infty [i(s) - i_b] s \, ds \tag{6}$$

The integral in (6) can be split as follows as:

$$Q = 2\pi \int_0^s [i(s) - i_b] s \, ds + 2\pi \int_{s_c}^\infty [i(s) - i_b] s \, ds \tag{7}$$

where s_c is an arbitrary spatial frequency value far greater than s_{max}, but inside the range of the experimental observation. The first of the two integrals in equation (7) is numerically calculable from the experimental data and, taking equation (5) into account, the second one becomes:

$$\int_{s_c}^\infty [i(s) - i_b] s \, ds = \int_{s_c}^\infty \frac{h_i}{s^2} \, ds = \frac{h_i}{s_c} \tag{8}$$

which is computable from the previously obtained data. Finally, the average diameter D is given by[16]:

$$D = \frac{Q}{\pi^3 h_i (1 - v_f)} \tag{9}$$

where v_f is the only parameter in equation (9) that cannot be extracted from Porod's analysis of the data.

The craze matter volume fraction, v_f, is usually obtained by means of optical density measurements and by comparison of the values obtained in the craze region, in the undeformed material and in a near hole[18]. We did not have the possibility to follow this method because the films under observation were too thick, making the optical density determination scarcely reliable, and, more importantly, reducing practically to zero the probability of finding an observable hole close to the crazes. In fact, the films were so brittle that, when a critical breakdown was reached in the fibrillar structure of the craze, it immediately developed into a catastrophic crack. The way we followed to determine v_f was, then, an indirect one. It is known that[18]:

$$\frac{D_0^*}{D} = \sqrt{\frac{1}{v_f}} \tag{10}$$

Combining equations (9) and (10) one obtains:

$$\sqrt{v_f}\,(1 - v_f) = \frac{Q}{\pi^3 h_i D_0^*} \tag{11}$$

The second term in (11) can be obtained from the data calculated from the Porod analysis of the spectra, so that v_f can be numerically computed by solving (11). However, there is a limitation: knowing that the volume fraction of the crazes is generally below 25% and that equation (11) allows a double solution for v_f, the solution has to be chosen in the range of v_f between 0 and 35%. Once that v_f is computed, D can easily be calculated from equation (9) or (10).

Table 4 contains the data of the Porod analysis of the spectra. Even though they are of the same order as the data previously reported for PS[18], some considerations have to be made. Only D_0^* comes from direct observation of the spectra (with the minimal limitation of the correction factor); the other parameters, D and v_f, instead come from quite a complex numerical analysis, containing a highly non-linear step [the solution of equation (11)], and consequently every speculation that makes use of these last two quantities has to be taken only in a semi-quantitative sense.

From the data reported in *Table 4*, it is readily observed that five of the seven HIPSs considered (materials B, C, E, F and G) have craze structural parameters largely different from those of the PS chosen as reference (material X).

It is important, for the aim of this work, to establish if this difference is due to the presence of the second phase or if it depends only on PS matrix characteristics, despite our attempt to maintain them the same in all the materials. In the second case, the difference should also stand if we remove the rubbery phase. For some of the considered materials, phase separation was obtained in the way described in the footnote in *Table 1* for the *gel* measurements. The dissolved part presumably contained the PS molecules and all the chemical species in it that

Table 4 Structural parameters of the crazes obtained from the Porod analysis[a]

	A*	B*	C*	D*	E*	F*	G*	X
D_0^*	24.0 ± 2.1	7.0 ± 0.5	7.6 ± 0.7	19.5 ± 2.5	8.2 ± 0.4	7.4 ± 0.4	7.3 ± 0.3	25.8 ± 3.7
$(D_0^*)_{m,MEK}$	33.3 ± 0.1	–	35.41 ± 4.2	–	–	30.65 ± 3.6	–	–
D	6.5 ± 0.1	3.0 ± 0.2	3.4 ± 0.2	4.8 ± 0.1	3.2 ± 0.1	2.8 ± 0.1	3.3 ± 0.2	5.4 ± 0.1
v_f	7.5 ± 2.1	28.5 ± 7.2	20.5 ± 7.6	6.5 ± 1.6	15.0 ± 3.2	14.0 ± 2.5	21.0 ± 5.8	5.0 ± 1.8
ρ	0.11	0.49	0.42	0.00	0.41	0.76	1.11	–

[a] The meaning of the symbols is given in the text. The corrected fibril spacing and diameter, D_0^* and D, are in nm; the craze volume fraction v_f is in %; the volumetric density of damage events ρ is in μm^{-3}. The subscripts m, MEK indicate that the data concern the pure matrix separated in MEK according to the procedure described in *Table 1*

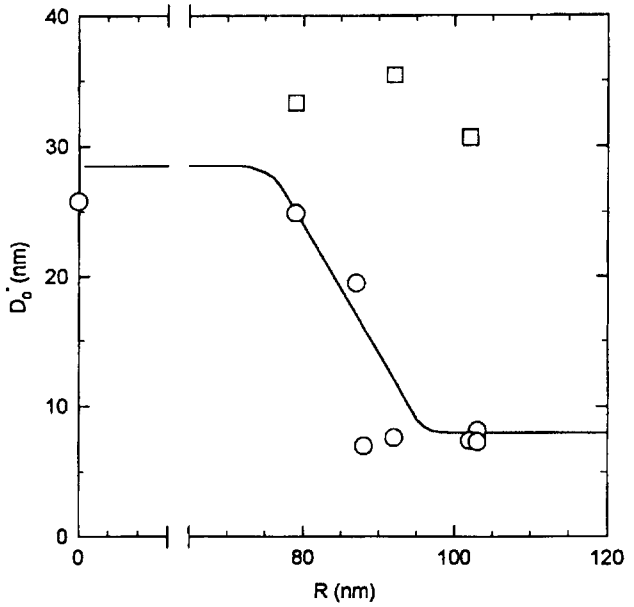

Figure 6 Plot of the average craze fibril spacing D_0^* *versus* the average rubber particle radius R for the considered HIPS materials: ○, from microtomed samples of diluted HIPSs; □, from pure matrices separated in MEK (see text and *Table 1*). The curved line is simply a guide for the eye

were soluble in MEK, but not the rubbery particles. The solutions were then spin-cast to produce thin films with a thickness of about 0.2–0.3 μm (greater thickness is difficult to realize by spin-casting). The obtained films were consequently strained and observed following the same technique reported above, yielding the structural data reported again in *Table 4*. *Figure 6* contains a plot of D_0^* *versus* R for the considered materials, showing also the data relative to matrices.

At this point we tried a quantitative analysis of the damage phenomenon that was observable in the HIPS crazes, as well. As mentioned above and has been previously reported, two kinds of damage can be observed in the HIPS crazes when core–shell particles are present. The first one involves some local fibril breakdown and appears to lacerate seriously the craze texture (Figure 2a in ref. 5), while the second one is seemingly limited to the particles, some of them becoming broken at their equator, considering as vertical the craze–bulk axis (Figure 2b in ref. 5). In general this second phenomenon is observed close to the midrib of the craze; however, a small percentage of broken particles not lying exactly on the midrib is occasionally observable.

We thus measured the volumetric density of damage events in the observed crazes ρ_f and ρ_p, using the equations:

$$\rho_f = \frac{N_f}{V_c} \tag{12}$$

$$\rho_p = \frac{N_p}{V_c} \tag{13}$$

where N_f and N_p are the number of broken fibril regions and broken particles, respectively, and V_c is the total craze volume observed. These data were computed using several pictures in which the observable craze width and length were measured and the thickness was assumed to be equal to the thickness of the film, which was about 1 μm. We believe that it could be interesting to evaluate the variation of a global parameter, ρ, defined as:

$$\rho = \rho_f + \rho_p \tag{14}$$

in the different materials. The values of ρ are reported in *Table 4* and plotted against R in *Figure 7*.

Due to the fact that the film thickness has not been measured, but only estimated during the microtoming phase of preparation by means of interference colours[8,9], the volumetric density data are certainly affected by a large experimental error. Furthermore, the phenomenon of damage can, in principle, depend strongly on the craze width: it is, in fact, reasonable to assume that if fibril breakdown is produced from arrested drawing in the presence of particles crossing the craze–bulk interface, the damage will increase with increasing craze width because the number of particles that cross the interface depends on the width itself. We leave further considerations of this fact to the Discussion part of this work.

Despite the limitations about stereological overlapping of particles in the pictures (mentioned above), we also found it interesting, from a qualitative point of view, to take a quick examination of the undiluted deformed samples. For this reason we prepared strained films of the undiluted samples in the same way as previously described. The phenomenon of entrapping, which in this case can be better described as the massive presence of the rubbery particles in the craze texture, was still visible and relevant.

Slow crack propagation experiments

To characterize the macroscopic fracture behaviour of the considered materials, we chose to perform slow crack propagation (SCP) experiments. It is now generally agreed that the phenomenon of SCP in notched specimens is reasonably well described for a wide range of

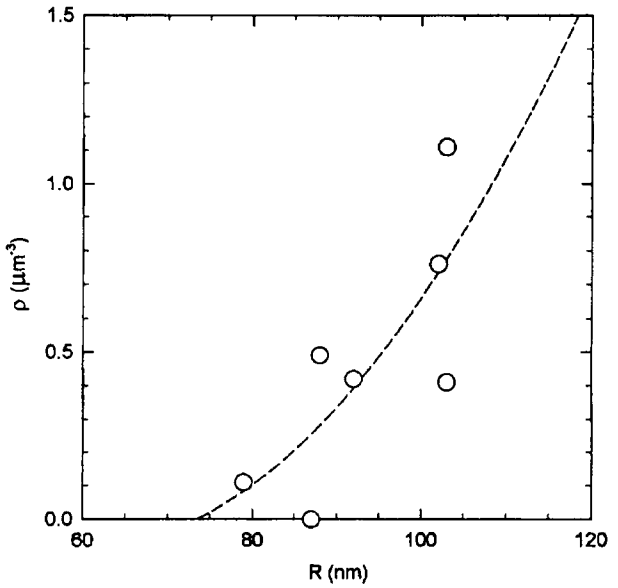

Figure 7 Plot of the total volumetric density of damage events ρ *versus* the average rubber particle radius R for the HIPS considered materials. The curve is simply a guide for the eye

materials, including the greatest majority of polymers, by the Paris law[30,32]:

$$\frac{da}{dt} = AK^m \tag{15}$$

where da/dt is the crack tip velocity at a given time, K the stress intensity factor at the same time, and A and m are two phenomenological constants that have to be extracted from the experimental data. In fatigue experiments the Paris law is often formulated using, instead of K, the K-difference in a cycle, ΔK. Utilization of the energy release rate G in equation (15) is also possible, due to the fact that K and G are, in the linear elastic case, simply related. Several observations suggest that in polymers at least m could be treated as material characteristic[32–38], and one of the authors of the present work recently proposed that both the Paris coefficients could be related to the microscopic features of the fracture, advancing the hypothesis that the coefficients could be extremely sensitive to the presence and structure of a dispersed phase[39].

SCP experiments were performed in our case in the following way. Compact tension (CT) specimens, having dimensions as reported in *Figure 8* and thickness of approximately 2 mm*, were obtained from compression moulded plates. A preliminary saw-cut notch was introduced and then the samples were treated by sputtering on a side surface a thin gold grid (mesh size of about 1 mm), aimed to work as a dimensional reference. Then the samples were annealed at about 80°C overnight in order to achieve the same physical ageing conditions; this precaution is due to the fact that the SCP experiments take a relatively long time and that

* The low thickness value is due to the fact that the materials were produced in very scarce quantities. Despite this fact we are confident, considering the relative brittleness of the HIPS used and the fact that crazing is certainly the only plastic deformation mechanism, that the fractures took place in plane stress conditions

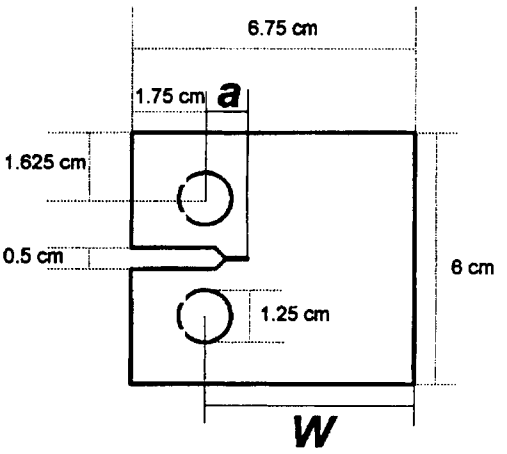

Figure 8 Sketch of the CT specimen used in the SCP experiments

samples produced at the same time could be consequently tested in very different moments.

Immediately before the mechanical tests, a razor notch was tapped at the pre-notch tip using a fresh razor blade for each sample, and at that time each specimen was tested in tension (mode I fracture) on a servo-hydraulic testing machine working under load control (by means of a feedback circuit on the load cell) with a load rate of approximately 0.17 N s^{-1}, which was the same for all the materials. At least three convincing samples were tested for each material. The choice to perform the experiments under load control was suggested by the fact that similar tests done simply by controlling the crosshead or the machine piston displacement can give rise to fracture slow down phenomena, due to the CT specimen soft form factor.

A camera with magnifying objective lenses of about 30× was used to follow the fracture advance: such a magnification was sufficient to enable good resolution of the crack tip position. The gold grid sputtered on the specimen was utilized as a dimensional reference, avoiding complicated calibration for the lenses' magnification factor (see above). The camera was mounted on a positioner device that allowed very small displacements, keeping the images still during the motion. The images were recorded on a VCR and synchronized to the load cell signal by means of a frame code generator. The frames were successively printed by means of a video printer and values of the fracture coordinate were simply obtained from the pictures. It was therefore possible to get sets of data relative to the position of the fracture on the side surface of the sample and to the applied load at the same instant for each fracture. Some preliminary, interrupted experiments demonstrated that, if the specimens were properly aligned (avoiding mode II and III components in the fracture process) and the razor notch was not oblique, the position of the fracture on the side of the specimen was coincident with the position in the bulk.

The K value at a given instant t was given by the equation[40,41]:

$$K(t) = f\frac{P(t)}{B \cdot \sqrt{W}} \tag{16}$$

where $P(t)$ was the applied load at the same time t, B the specimen thickness, the meaning of W is illustrated in

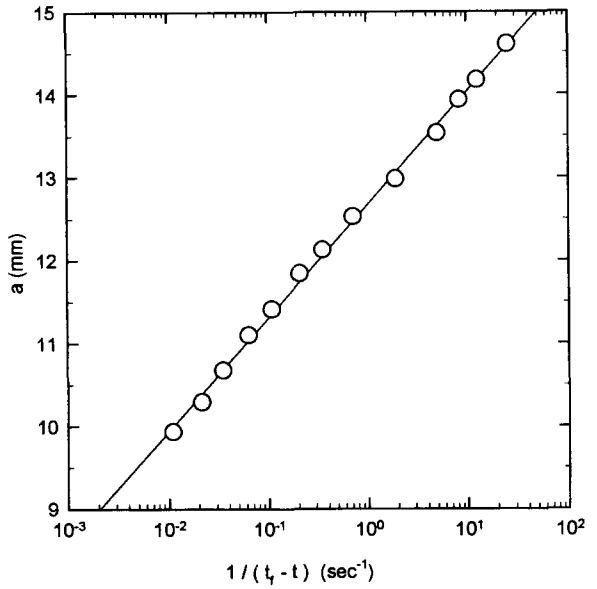

Figure 9 Plot of the crack coordinate a *versus* $1/(t_f - t)$ (logarithmic scale) for a single SCP experiment. Data relate to material E. The line is a regression on the logarithmic data

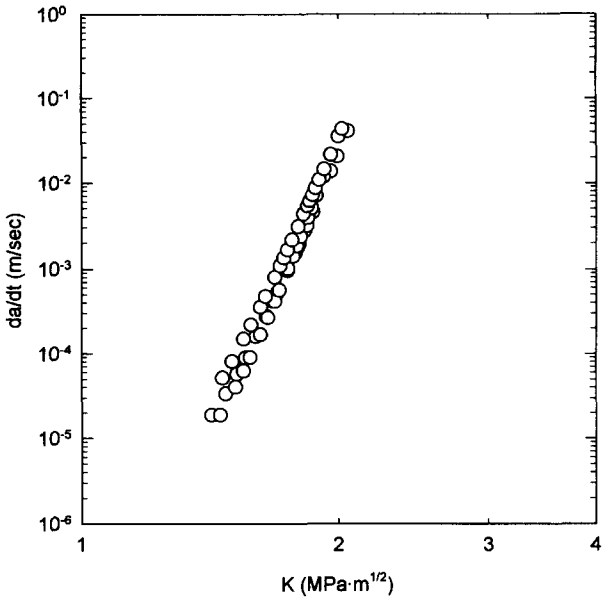

Figure 10 Paris plot for material F

Figure 8 and f is given by:

$$f = \frac{2+\frac{a}{W}}{\sqrt{\left(1-\frac{a}{W}\right)^3}}\left[0.886 + 4.64\left(\frac{a}{W}\right) - 13.32\left(\frac{a}{W}\right)^2 + 14.72\left(\frac{a}{W}\right)^3 - 5.6\left(\frac{a}{W}\right)^4\right] \quad (17)$$

where a, which is also time-dependent, represents the fracture coordinate (*Figure 8*). Equations (16) and (17) hold when $0.2 < a/W < 0.8$: data outside this range were never considered.

For determination of the crack speed we adopted the following method. Quite generally we observed that the plot of the measured $a(t)$ values *versus* $\log[1/(t_f - t)]$,

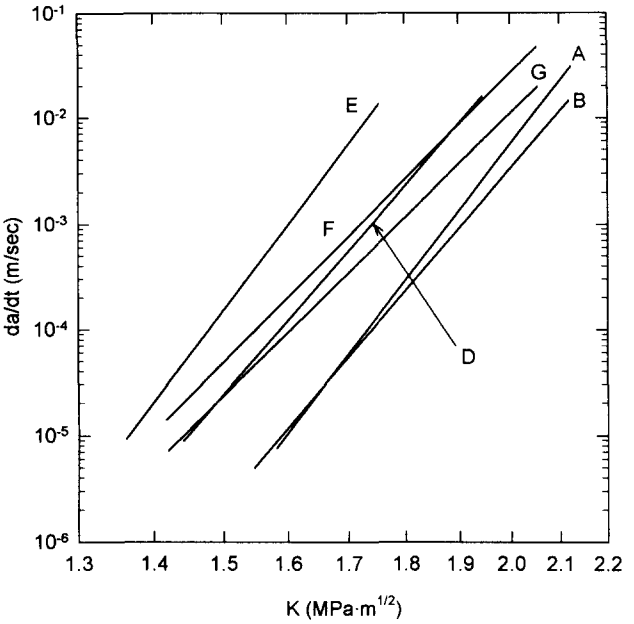

Figure 11 Paris plots for the considered materials (only linear regressions in log–log scale are displayed)

where t_f is the total fracture time, were well defined straight lines (*Figure 9* is a typical example). It is possible then to write:

$$a(t) = M + N\log\left(\frac{1}{t_f - t}\right) \quad (18)$$

where M and N are constants that can be obtained from the experimental data relating to each sample. It is easy to conclude, then, that:

$$\frac{da(t)}{dt} = \frac{N}{t_f - t} \quad (19)$$

At this point the Paris plots of $da(t)/dt$ *versus* $K(t)$ are easily attainable for each sample.

Figure 10 contains a typical Paris plot for one of the considered HIPSs, *Figure 11* gives a sketch of the global situation, while *Table 5* shows the Paris coefficients, simply obtained by power regressions, together with their correlation factors. *Table 5* also contains data for material X obtained in a previous experimentation in the same conditions, but with a different experimental set-up. The much lower correlation factor shows that in this case a large experimental error was present in the data.

DISCUSSION

We can, at this point, discuss the experimental evidence gathered so far.

The yielding mechanisms should be influenced by the presence of the second phase due to the fact that, from a continuum mechanics point of view, the rubbery particles act as stress concentrators and thus lower the macroscopic yielding threshold of the material. The stress concentration around a simple spherical particle has been computed in a classical work by Goodier[42]; however, calculation of the stress concentration in a real material with a population of dispersed spheres (such as HIPS) would require consideration of the mutual

Table 5 Paris coefficients[a]

	A	B	C	D	E	F	G	X
A	2.5×10^{-11}	7.7×10^{-11}	–	1.1×10^{-9}	1.4×10^{-9}	6.6×10^{-9}	3.8×10^{-9}	1.8×10^{-5}
m	27.72	25.39	–	24.72	28.65	21.98	21.48	8.25
r^2	0.94	0.98	–	0.98	0.98	0.98	0.98	0.80

[a] The meaning of the symbols is given in the text [equation (32)]; r^2 is the regression correlation factor. Due to the power nature of the Paris law, A and m have variable dimensions. The obtained values are for the stress intensity factors in MPa $m^{1/2}$ and the crack speeds in m s^{-1}

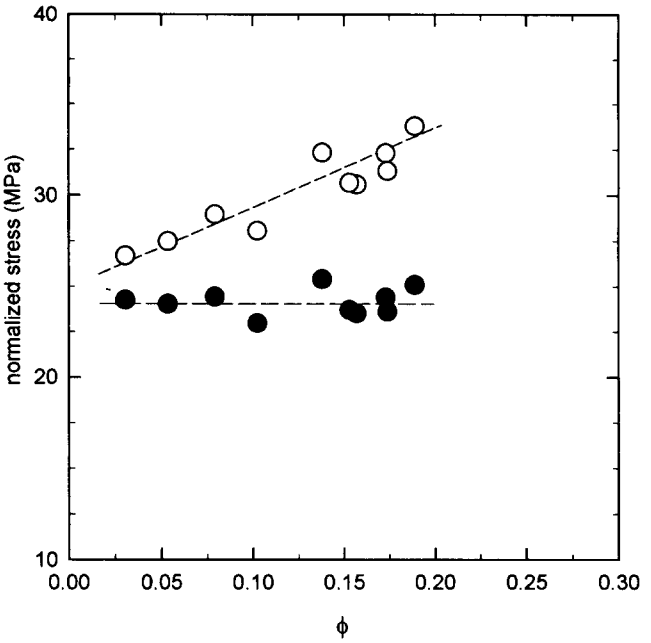

Figure 12 Plot of the normalized stress at yield *versus* the second phase volume fraction ϕ for the considered HIPS materials: ○, relate to the stress normalization according to the Ishai and Cohen [equation (22) in the text]; ●, to the stress normalization according to the Delesse and Rosiwal stereological principle [equation (23) in the text]. The dashed lines are simply guides for the eye

co-operative effects of the different spheres, something which is practically impossible in analytical terms and prohibitive also from the numerical point of view. A similar approach is the one first proposed by Ishai and Cohen[43] and then successfully applied to acrylonitrile–butadiene–styrene (ABS), which is structurally very similar to HIPS[10,44]. In the Ishai and Cohen model the dispersed particles are assimilated to holes arranged in a regular cubic lattice and the stress concentration is plainly neglected. In fact, the composite yield stress is obtained from the matrix yield stress taking into account that the effective sample sections is reduced in the composite, with respect to the macroscopic value, by the presence of the second phase. If we call S_0 the macroscopic sample section, S_E the effective section occupied by the matrix and, as above, ϕ the second phase volume fraction, it is easy to demonstrate that, in a lattice plan under the Ishai and Cohen conditions:

$$\frac{S_0}{S_E} = \left(1 - \sqrt[3]{\frac{9\pi}{16}\phi^2}\right)^{-1} \tag{20}$$

and then that the yielding stress of the composite, σ_y, is given by:

$$\sigma_y = \sigma_0 \cdot \left(1 - \sqrt[3]{\frac{9\pi}{16}\phi^2}\right) \tag{21}$$

where σ_0 is the matrix yielding stress.

In many cases the matrix by itself is very brittle and experimental assessment of the value of σ_0 is virtually impossible. It is then useful, in order to check the validity of the approach, to produce plots of the normalized stress, $\sigma_y\gamma$ *versus* ϕ, where γ is:

$$\gamma = \left(1 - \sqrt[3]{\frac{9\pi}{16}\phi^2}\right)^{-1} \tag{22}$$

If the plots show horizontal lines corresponding to values that can be reasonably attributed to the matrix yield stress, one can conclude that the Ishai and Cohen model describes sufficiently well the yielding phenomenon in the considered materials. However, the Ishai and Cohen approach is not applicable to the case of the core–shell HIPS: the plot of $\sigma_y\gamma$ *versus* ϕ (empty circles in *Figure 12*) gives rise to a line whose slope is definitely not zero. Furthermore, taking into account that the yielding point in HIPS materials corresponds to the moment when the crazes, macroscopically observable as a whitening in the specimen, diffuse through the entire cross-section[45], and that experiments performed by us on material X produced values of the stress at break not higher than 25 MPa, then $\sigma_y\gamma$ reaches values that cannot reasonably be attributed to the matrix yielding.

This outcome is not surprising: there is an assumption in the Ishai and Cohen model which can hardly fit to disordered dispersion, as our case is likely to be—namely that the particles lie on a regular cubic lattice. Nonetheless it is possible to retain one of the Ishai and Cohen assumptions, i.e. the hypothesis that no stress concentration takes place around the particles, and to model the spatial distribution of the second phase in a more realistic way. According to Delesse and Rosiwal principle, which is a very basic rule of stereology, the volume fraction of a second phase randomly embedded in a structure is equal, under some very broad conditions, to its areal fraction obtained on an ideal section (i.e. on a section with zero thickness)[46]. Equation (20) can then be rewritten as:

$$\frac{S_0}{S_E} = (1 - \phi)^{-1} \tag{23}$$

The concept of normalized stress can be adapted to this case: we have simply to adopt a different factor, δ, given by the right term in equation (23). We expect, then, that $\sigma_y\delta$ *versus* ϕ originates a horizontal line. *Figure 12* shows that this is the case: the solid circles are, indeed,

contained in a narrow horizontal region from about 23 to about 26 MPa. This interval is of the same order of magnitude as the experimental error for yielding experiments, especially when low values of ϕ are considered, and sounds proper as a yielding stress value for the matrix.

The fact that no stress concentration around the particles takes place is confirmed by the TEM evidence that craze nucleation is not enhanced by the dispersed phase. This fact, which is in open contrast to the conclusion of the continuum elastic theory, has been explained in the past by means of the hypothesis that the stress concentration could be effective only if it spans a region of the order of some craze fibrils, which is not the case for the core–shell particles[25]. We believe, more generally, that in the case of small rubber particles the dimensions involved in the stress transfer phenomena are too close to the characteristic molecular dimensions, like for example the gyration radius; for this reason application of the continuum elasticity theory could be excessively strained. Furthermore, we believe that fast relaxation processes taking place at the PS–PB interface and responsible for the stress lowering cannot be easily excluded.

On the other hand, examination of the craze features in the diluted samples poses some other problems: the main one due to the fact that the fibril spacing seems to decrease with increasing particle size, and that this variation does not happen in samples in which the rubbery phase has been removed by means of selective solution. This result has an important consequence. Let us consider, for instance, the relationship derived by Kramer[18]:

$$SD_0^* = \frac{8\Gamma}{\beta} \tag{24}$$

where the new symbols S, Γ and β represent the tensile stress on the craze surface averaged on several fibrils, the surface energy at the craze–bulk interface and a constant lower than 1, respectively. The inverse of the fibril spacing then corresponds to the term $S\beta/8\Gamma$ that, considering that there are no reasons for Γ to vary, should represent the drawing stress at the craze–bulk interface. At this point it is possible to conclude, following our results, that this quantity should increase in a discontinuous way when the particle radius reaches a value of approximately 90 nm.

It would be fascinating to imagine that, when the particles are swallowed at the craze–bulk interface, they can increase the drawing stress; however this hypothesis is not convincing. Reasons are hard to find that explain why slightly smaller particles are swallowed without consequence, while bigger ones could produce such a dramatic increase in the drawing stress. Furthermore, our measurements of the craze's features were done in regions in which no entrapped particles were present, while a phenomenon of drawing stress amplification due to entrapping should not cover a region much larger than the one occupied by the absorbed particle.

At the present moment, we propose than an explanation of the fibril spacing reduction can be found in increased fibril coalescence. Due to the fibril breakdown phenomenon, which is certainly much more relevant when the particle size increases, we can imagine that the fibrils can come closer to one another, having lost any possibility to bear transverse stress. In this coalescence a role can be played also by the cross-tie fibrils[19]: they exert a force in the direction perpendicular to the drawing direction and then, when the connection from the fibril and the bulk is interrupted by a rubber particle crossing the interface, tend to heap the fibrils up with the possibility to produce bundles. We cannot, however, consider this explanation as definitive either, and we propose it here to further research developments.

The craze texture damage, on the contrary, is measured in a much more direct way and the results described in the previous section can be considered qualitatively reliable, with only one limitation, due to the difficulty in taking long-range examination, that the resulting data are poorly averaged. It is interesting, nonetheless, to try some elaboration of these data and to explore the possibility of finding a correlation with the SCP features.

The craze damage measurements were done on strained films: they did not contain any initial sharp crack or artificial stress concentrator such as a notch, so in this case it is difficult to apply the idea of the stress intensity factor; although we can imagine that, when the craze forms and propagates, a singularity in the stress field could be supposed at the craze tip. We can use then the Paris coefficients, previously calculated, to compute the value of the hypothetical crack speed corresponding to a very low stress intensity factor, assuming that this could be a condition close to the one of the strained thin films.

Before doing so a clarification has to be made. The fact that no stress intensification is produced by the particles suggests that the stress intensity factor, as measured by equation (16), should be considered only as a nominal value, being necessarily a normalization (similar to that proposed for the yielding values) in order to take into account the presence of the second phase. The normalized stress intensity factor K_n is then easily given by:

$$K_n = K(1-\phi)^{-1} \tag{25}$$

Figure 13 is a plot of the crack speed [corresponding to a K_n value of 0.5 MPa $m^{1/2}$, which is well below the matrix critical stress intensity factor (that for material X is about 2.0 MPa $m^{1/2}$, measured according to refs 40 and 41)] with respect to the volumetric density of fibril damage ρ, previously defined [equation (14)] for the considered materials. With the only anomaly of material D, the data show a sharp increasing tendency, demonstrating that the fibril damage phenomenon is related to the crack propagation in a quite strict way. Moreover, we do not consider the discrepancy introduced by the material D excessively relevant, taking into account the possibility of large experimental scatter (as previously mentioned) and the fact that the degree of crosslinking of the rubbery phase, indirectly measured by the so-called swelling index (*Table 1*), can also play a role in the SCP behaviour. This latter aspect will be discussed further below.

To develop further the notion of a relationship between crack propagation and craze damage, we have to recall briefly here some ideas which have been presented by one of us in ref. 39.

First of all, we assume that in a notched specimen the crack tip velocity should be proportional to the craze

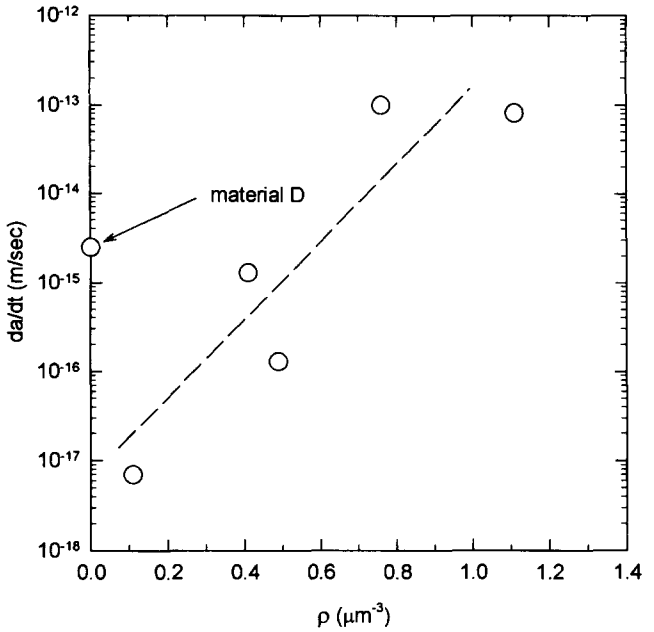

Figure 13 Plot of the crack speed da/dt (corresponding to a value of the normalized stress intensity factor of 0.5 MPa m$^{1/2}$) *versus* the total volumetric density of damage events ρ for the HIPS considered materials. The dashed line is simply a guide for the eye

fibril breakdown probability p_{bd} at the crack–craze interface:

$$\frac{da}{dt} \propto p_{bd} \tag{26}$$

Yang *et al.*[2] demonstrated that the craze fibril breakdown probability can be easily modelled by means of a Weibull distribution[47,48] in the plastic strain ε_p, defined as the difference between the actual strain and the strain for craze nucleation:

$$p_{bd}(\varepsilon_p) = 1 - \exp\left[-\left(\frac{\varepsilon_p}{w_1}\right)^{w_2}\right] \tag{27}$$

where w_1 and w_2 are the Weibull distribution coefficients. Maestrini proposed that equation (27) can be restated, in the case of a notched specimen of a craze-prone material fracturing in mode I, in terms of craze opening displacement h and a size parameter of the specimen[39]. Then, by means of the Dugdale–Barenblatt model, which is now well documented to be a good description of the shape and size of the crazed zone at the crack tip[49–55], it is possible to express the craze opening displacement in terms of the stress intensity factor:

$$h = \frac{K^2}{\sigma_c E^*} \tag{28}$$

where σ_c is the compressive stress that counterbalances the crazing stress in the plastic zone (its value is, of course, equal to that of the crazing stress) and E^* is the reduced Young's modulus, that in plane stress coincides with the Young's modulus.

One obtains then an equation for the crack speed of the form:

$$\frac{da}{dt} \propto 1 - \exp\left[-\left(\frac{K^2}{w_1' \sigma_c E}\right)^{w_2}\right] \tag{29}$$

We stress here that the use made of the Dugdale model is free from the major criticism it has encountered in the application to craze-prone polymers. The model, in fact, does not provide a criterion for crack advance and the critical opening displacement criterion is often introduced *a posteriori* in the description, disregarding the fact that a true critical craze opening displacement can hardly exist for crazes which widen by surface drawing[56]. In our approach, instead, only the geometrical features of the model—which are largely accepted—are applied.

In the case (which is extremely probable in macroscopic experiments[39]) that the exponential argument in equation (29) is much lower than 1, one has, by means of a commonplace Taylor approximation, a Paris-like equation for the crack speed:

$$\frac{da}{dt} \propto \left(\frac{1}{w_1' \sigma_c E}\right)^{w_2} K^{2w_2} \tag{30}$$

It is clear from the mathematical derivation that equation (30) is referred to the case of a single-phase material. The problem now is to adapt it to the presence of a dispersed phase and to apply it to our HIPS materials. Due to the fact that the core–shell particles do not produce stress intensification, the values of the crazing stress and the stress intensity factor, which are local quantities, have to be related to the matrix only. σ_c will have the same values for all the considered materials, while it will be necessary to introduce, instead of the nominal stress intensity factor, the normalized one [equation (25)] in equation (30). The value of the elastic modulus—which is, on the other hand, a global quantity—has to be that of the composite material, the effect of the second phase being relevant to the elastic characteristics.

After that, we can easily express the two Weibull coefficients in terms of the Paris constants that have been computed for the HIPS materials:

$$w_1' \propto [A^{2/m} E (1-\phi)^2]^{-1} \tag{31}$$

$$w_2 = \frac{m}{2} \tag{32}$$

Yang *et al.*[2] stated that the first Weibull coefficient, which can be defined as a scale parameter, is proportional to the difference between the breakdown strain and the crazing strain for the material, $\varepsilon_b - \varepsilon_c$.

More interesting to us is to understand in which way the morphological and structural characteristics of the HIPS materials affect the second Weibull coefficient and, consequently, the Paris exponent m, which is considered a material characteristic[32–38]. Yang *et al.*[2] proposed a physical meaning for the coefficient w_2, which they called the Weibull modulus, in terms of a breakdown seed density. The Weibull modulus is interpreted as representing the distribution of effectiveness of the breakdown seeds, including dust particles, weak spots and, in our case, also the rubbery particles that should have a much greater influence than the other, accidental factors. We noticed that bigger particles tend to produce more craze damage. Of course increasing the number of the particles and then volumetric concentration, we can expect that the craze damage would correspondingly increase. This hypothesis is not contradicted by the few TEM observations we made of the undiluted HIPS. It is possible to imagine, then, that the effectiveness of the fracture

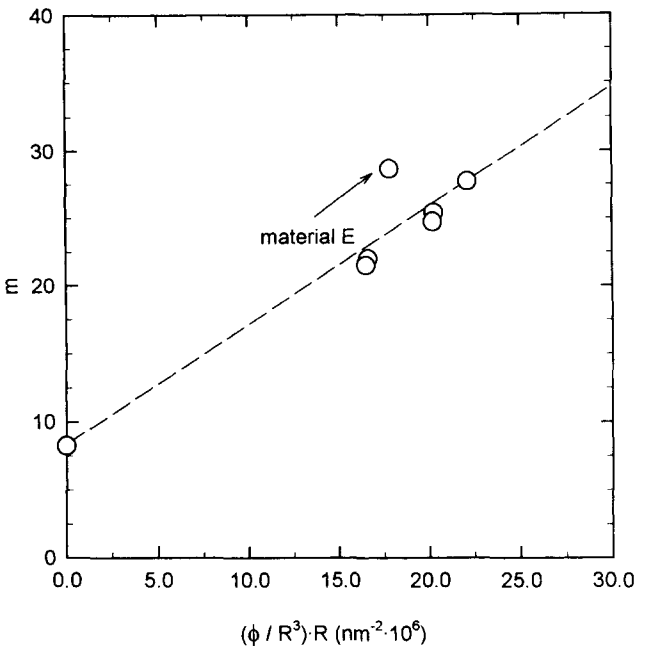

Figure 14 Plot of the Paris exponent *m versus* $(\phi/R^3)R$ for the HIPS considered materials. The dashed line is simply a guide for the eye

seeds only depends on:

- the size of the rubber particles;
- the concentration of the rubber particles.

Assuming that these two factors are coupled and that the dependence of the size is the simplest possible, i.e. a linear one, we can write:

$$m \propto \left(\frac{\phi}{R^3}\right)R \tag{33}$$

where the first term on the right-hand side of equation (33) represents the concentration contribution and the second the size contribution to the damage statistics.

Figure 14 is a plot of *m versus* $(\phi/R^3)R$. It is easy to check that, with the only exception of material E, the data are very well arranged on a line that includes also the matrix (for which it is assumed an abscissa value of zero). This evidence, with the obvious limitations that can be attached to it, confirms the idea that a relationship exists between the microscopic damage phenomena that takes place in HIPS and the macroscopic SCP behaviour.

Some considerations have to be made, at this point, on materials D and E, which twice introduced anomalies in the previous discussion. The first one (D) shows a peculiarly low craze damage parameter measured on the diluted samples, while the second one (E) has a Paris exponent higher than that expected on the basis of its structural and morphological characteristics. The two materials, however, show extreme values of the swelling index (SI) (*Table 1*)—very high for material D and very low for material E—and, if we consider that the SI is an indirect measure of the degree of crosslinking of the rubbery phase (the higher the SI, the lower the crosslinking degree), we can possibly find an explanation to the behaviour of these two materials.

We can imagine, in fact, that poorly crosslinked particles can cross the craze–bulk interface with a higher probability of maintaining intact the craze texture, while highly crosslinked ones can produce much more relevant damage. This explains why in material D no craze damage was observable, while the fracture statistics was more pronounced in material E.

From our SCP and microscopic experimental evidence it is also possible to state, without any doubt, that the presence of a rubbery phase with characteristics described in the present work is detrimental to the fracture propagation mechanisms. Therefore, any understanding of the matrix toughness improvement resulting from the addition of small particles, when characterized by ordinary tests such as the notched Izod impact test, must necessarily depend on the fracture initiation phase, which is present, and probably predominant, when a rounded notch (or no notch at all) is considered.

In conclusion we have to add that the described approach, which is developed here from the idea of the statistics of craze fibril breakdown, can possibly be extended to more general situations. We believe that the fact that the crack speed could be related to the plastic strain in an exponential way does not need to be interpreted solely in a statistical manner, opening the possibility to extend the approach to different classes of materials in which the concept of purely statistical fracture is not realistic.

CONCLUSIONS

The main conclusions of the present work may be summarized as follows.

1) The stress concentration produced by the considered core–shell particles, which have average radius of less than 100 nm, is not effective to enhance craze nucleation.
2) The core–shell particles do not stop crazes but, instead, are swallowed by them. When they are entrapped in the craze structure, they produce a quantity of damage (fibril breakdown) which increases with increasing particle size and volume fraction of the second phase. The examined particle sizes were all in a range in which no craze nucleation and/or stopping were observed.
3) It is possible to correlate the microscopic craze damage with the macroscopic fracture behaviour. Namely, it is useful to model the craze fibril fracture by means of a Weibull statistical distribution containing two parameters and to write a relationship between the Weibull statistics and the Paris law for SCP.
4) The second Weibull coefficient, which is proportional to the Paris exponent, is related to the distribution of effectiveness of the breakdown seeds: it increases (and then the fracture propagation becomes more critical) when the concentration and size of the rubbery particles increase (within the obvious limitations of the sizes and morphologies discussed here).
5) The idea that the crack speed can depend in an exponential way on the plastic strain is not limited only to a statistical description of the fracture. The approach presented here could, then, be extended to a wider class of materials.

ACKNOWLEDGEMENTS

Experimental assistance from A. Callaioli, K. Pisoni and M. Vighi (EniChem) is gratefully acknowledged. C.M.

thanks Enichem for the use of its lab in performing this work, which was completed in partial fulfilment of the requirements for the degree of Docteur ès Sciences Téchniques at EPFL.

REFERENCES

1 Kambour, R. P. *Nature* 1962, **195,** 1299
2 Yang, A. C. M., Kramer, E. J., Kuo, C.C. and Phonenix, S. L. *Macromolecules* 1986, **19,** 2010
3 Bucknall, C. B. and Smith, R. R. *Polymer* 1965, **6,** 325
4 Bucknall, C. B. 'Toughened Plastics', Applied Science Publishers, London, 1977
5 Maestrini, C., Castellani, L., Merlotti, M. and Vighi, M. *Polymer* 1992, **33,** 1556
6 Echte, A. in 'Rubber Toughened Plastics' (Ed. C. K. Riew), American Chemical Society, Washington, 1989
7 Echte, A. *Angew. Makromol. Chem.* 1975, **58/59,** 175
8 Maestrini, C., Merlotti, M., Vighi, M. and Malaguti, E. *Proc. EPF '92*, Baden Baden, 1992
9 Maestrini, C., Merlotti, M., Vighi, M. and Malaguti, E. *J. Mater. Sci.* 1992, **27,** 5994
10 Giaconi, G. F., Castellani, L., Maestrini, C. and Riccò, T. *Proc. 10th IGF*, Torino, 1994
11 Kato, K. *Polym. Eng. Sci.* 1967, **7,** 38
12 Kambour, R. P. and Holik, A. S. *J. Polym. Sci.* 1969, **A2,** 1393
13 Kambour, R. P. and Russel, R. R. *Polymer* 1971, **12,** 237
14 Lauterwasser, B. D. and Kramer, E. J. *Phil. Mag.* 1979, **A39,** 1979
15 Brown, H. R. and Kramer, E. J. *J. Macromol. Sci. Phys.* 1981, **B19,** 987
16 Brown, H. R. *J. Polym. Sci., Polym. Phys. Edn* 1983, **21,** 483
17 Yang, H. C. M. and Kramer, E. J. *J. Polym. Sci., Polym. Phys. Edn* 1985, **23,** 1353
18 Kramer, E. J. *Adv. Polym. Sci.* 1983, **52/53,** 1
19 Kramer, E. J. and Berger, L. L. *Adv. Polym. Sci.* 1990, **91/92,** 1
20 Donald, A. M. and Kramer, E. J. *Polymer* 1981, **22,** 691
21 Donald, A. M. and Kramer, E. J. *J. Polym. Sci., Polym. Phys. Edn* 1982, **20,** 899
22 Donald, A. M. and Kramer, E. J. *Polymer* 1982, **23,** 461
23 Donald, A. M. and Kramer, E. J. *J. Mater. Sci.* 1982, **17,** 1871
24 Donald, A. M. and Kramer, E. J. *J. Mater. Sci.* 1982, **17,** 2351
25 Donald, A. M. and Kramer, E. J. *J. Appl. Polym. Sci.* 1982, **27,** 3729
26 Yang, A. C. M. and Kramer, E. J. *J. Mater. Sci.* 1986, **21,** 3601
27 Porod, G. *Kolloid Z.* 1951, **124,** 83
28 Porod, G. *Kolloid Z.* 1952, **125,** 109
29 Maestrini, C. and Kramer, E. J. *Polymer* 1991, **32,** 609
30 Paris, P. C. *Proc. 10th Sagamore Conf.*, Syracuse, 1964
31 Hertzberg, R. W. and Manson, J. A. 'Fatigue of Engineering Plastics', Academic Press, London, 1980
32 Hertzberg, R. W. and Manson, J. A. in 'Encyclopedia of Polymer Science and Engineering (Vol. 10)', John Wiley & Sons, New York, 1985
33 Hertzberg, R. W., Manson, J. A. and Skibo, M. D. *Polym. Eng. Sci.* 1975, **15,** 252
34 Hertzberg, R. W., Skibo, M. D. and Manson, J. A. *ASTM STP 700*, American Society for Testing and Materials, Philadelphia, PA, 1980
35 Williams, J. G. 'Fracture Mechanics of Polymers', Ellis Horwood, Chichester, 1984
36 Kim, S. L., Skibo, M. D., Manson, J. A. and Hertzberg, R. W. *Polym. Eng. Sci.* 1977, **17,** 194
37 Michel, J. C., Manson, J. A. and Hertzberg, R. W. *Am. Chem. Soc. Polym. Prepr.* 1985, **26,** 141
38 Bucknall, C. B. and Faitrouni, T. *Proc. 8th Def. Yield. Fract. Polym.*, Cambridge, 1991
39 Maestrini, C. *Polymer* 1992, **33,** 3076
40 Williams, J. G. and Cawood, M. J. *Polym. Test.* 1990, **9,** 15
41 European Group on Fracture, *EGF Newsletter* Winter 1986/1987, **1**
42 Goodier, J. N. *J. Appl. Mech.* 1933, **55,** 39
43 Ishai, O. and Cohen, L. *J. Compos. Mater.* 1968, **2,** 302
44 Riccò, T., Rink, M., Caporusso, S. and Pavan, A. *Proc. 2nd Tough. Plast.*, London, 1985
45 Castellani, L., Maestrini, C. and Merlotti, M. *Proc. 8th Def. Yield. Fract. Polym.*, Cambridge, 1991
46 Weibel, E. R. 'Stereological Methods', Academic Press, New York, 1979
47 Weibull, W. *Ing. Vetenskaps Akad. Handl.* 1939, **151,** 1
48 Weibull, W. *J. Appl. Mech.* 1951, **18,** 293
49 Dugdale, D. S. *J. Mech. Phys. Solids* 1960, **8,** 100
50 Barenblatt, G. I. *Adv. Appl. Mech.* 1962, **7,** 55
51 Brown, H. R. and Ward, I. M. *Polymer* 1973, **14,** 469
52 Weidmann, G. W. and Döll, W. *Colloid Polym. Sci.* 1976, **254,** 205
53 Mills, N. J. and Walker, N. *Polymer* 1976, **17,** 439
54 Morgan, G. P. and Ward, I. M. *Polymer* 1977, **18,** 1987
55 Fraser, R. A. and Ward, I. M. *Polymer* 1977, **19,** 220
56 Kramer, E. J. and Hart, E. W. *Polymer* 1984, **25,** 1667